



ARTICLE OPEN

Direct observation of broadband nonclassical states in a room-temperature light–matter interface

Jian-Peng Dou^{1,2}, Ai-Lin Yang^{1,2}, Mu-Yan Du¹, Di Lao¹, Hang Li^{1,2}, Xiao-Ling Pang^{1,2}, Jun Gao^{1,2}, Lu-Feng Qiao^{1,2}, Hao Tang^{1,2}  and Xian-Min Jin^{1,2} 

Nonclassical state is an essential resource for quantum-enhanced communication, computing and metrology to outperform their classical counterpart. The nonclassical states that can operate at high bandwidth and room temperature while being compatible with quantum memory are highly desirable to enable the scalability of quantum technologies. Here, we present a direct observation of broadband nonclassical states in a room-temperature light–matter interface, where the atoms can also be controlled to store and interfere with photons. With a single coupling pulse and far off-resonance configuration, we are able to induce a multi-field interference between light and atoms to create the desired nonclassical states by spectrally selecting the two correlated photons out of seven possible emissions. We explicitly confirm the nonclassicality by observing a cross correlation up to 17 and a violation of Cauchy–Schwarz inequality with 568 standard deviations. Our results demonstrate the potential of a state-built-in, broadband and room-temperature light–matter interface for scalable quantum information networks.

npj Quantum Information (2018)4:31 ; doi:10.1038/s41534-018-0083-1

INTRODUCTION

Quantum information network, large enough to be capable of carrying out quantum technologies^{1–4} beyond classically possible, is composed of two key elements: the nonclassical state carrying flying qubit and quantum memory as the node of storing stationary qubit. An efficient architecture requires both nonclassical state and quantum memory to have high fidelities, mutually compatible light–matter interfaces, and preferably to have the capabilities of running at high speed and room temperature conditions.^{5,6}

Albeit there are advances of pushing bandwidth from narrow-band to broadband and storage media from ultra-cold atomic gas to room-temperature atomic vapor,^{7–17} it is not until recently that the room-temperature broadband memories being capable of operating with a high fidelity genuinely in quantum regime were achieved.^{18,19} However, the spectrum of conventional optical down conversion by pumping a nonlinear crystal is still too large to match the acceptance bandwidth of quantum memories. Although a cavity can be added to shape the spectra and enhance the efficiencies of down converted photons, it is extremely challenging to align and maintain the nonclassical state generation highly efficient and stable.^{9,20,21} Moreover, the specially built state generation systems and their complexities make quantum networks physically hard to scale up.

In case of the nonclassical state that can be directly obtained by employing the same atomic ensemble and similar light–matter interaction mechanism with quantum memory, the resulting naturally matched emission line and bandwidth will make quantum networks elegant and straightforward to build. In the last 15 years, many works have successfully demonstrated nonclassical state (heralded single photons or photon pair sources) generations in cold atoms.^{10,22–25} However, the room-

temperature and broadband features are more appealing and essential for being compatible with high-speed and physically scalable quantum technologies, and meanwhile have been proven very challenging.^{26–28} The previous experiments with small detuning in room-temperature atoms suffer from fluorescence noise induced by Doppler effect and atom–atom collision. The broadband nonclassical correlation can be observed by continuously addressing ladder-type hot atoms, which is, however, not directly usable due to the random creation time of correlated photons and the distinctly different interaction mechanism with Raman process of broadband quantum memory.^{29,30}

In this work, we present a multi-field light–matter interference induced by a far-off resonance short coupling pulse. We have addressed all these open questions by realizing nonclassical discrete-variable states generation and measurement at pulse mode, broad bandwidth, and room temperature. Furthermore, the collinear configuration realized in our experiment may be used for long lifetime quantum memory due to minimization of spin wave dephasing.

RESULTS

The far off-resonance and Λ -type configuration shown in Fig. 1a are the two main features that our scheme shares with Raman¹⁶ and FORD¹⁹ broadband quantum memory. The two lower states $|1\rangle(6S_{1/2}, F=3)$ and $|3\rangle(6S_{1/2}, F=4)$ are the hyperfine ground states of ^{133}Cs with a frequency difference of 9.19 GHz, and the upper state $|2\rangle$ is the excited state that we mark at the cross over between $6P_{3/2}$, $F'=4$ and $F'=5$ as a precise reference. We initialize all atoms to the state $|1\rangle$ by a pump light in the transition of $|3\rangle$ and $|2\rangle$, and temporally switch off the pump by an acoustic optical modulator. We apply a single linearly polarized and 2 ns

¹State Key Laboratory of Advanced Optical Communication Systems and Networks, School of Physics and Astronomy, Shanghai Jiao Tong University, 200240 Shanghai, China and

²Synergetic Innovation Center of Quantum Information and Quantum Physics, University of Science and Technology of China, 230026 Hefei, Anhui, China

Correspondence: X.-M. Jin (xianmin.jin@sjtu.edu.cn)

Received: 24 January 2018 Revised: 20 June 2018 Accepted: 3 July 2018

Published online: 20 July 2018

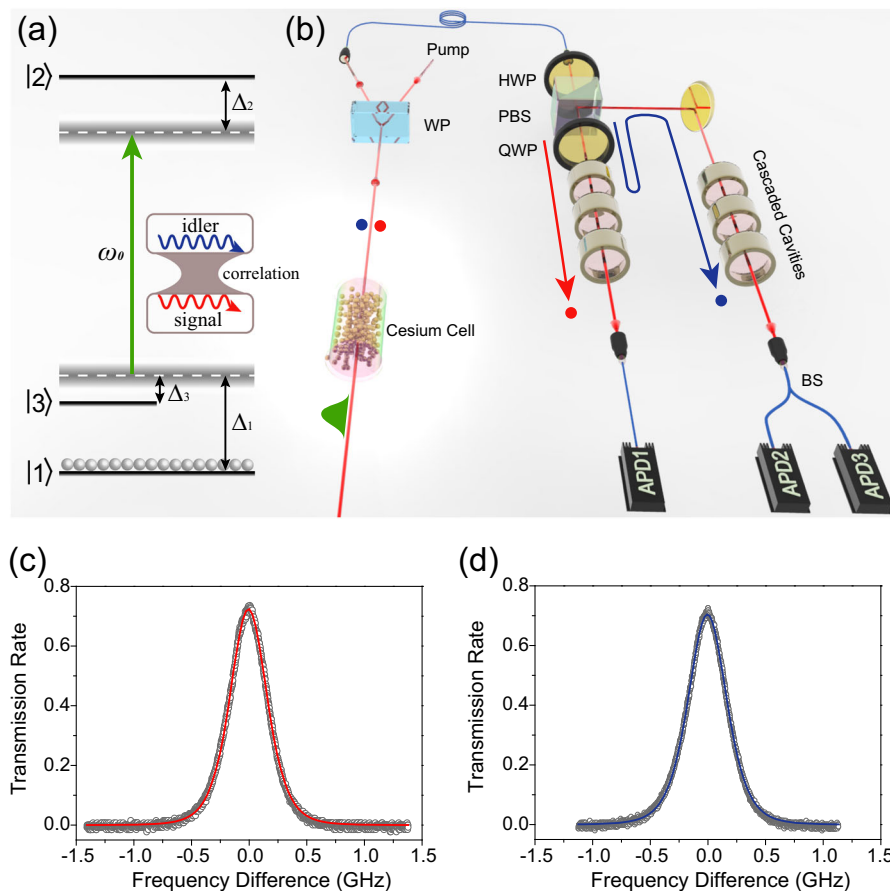


Fig. 1 Schematic view of the experiment. **(a)** Energy-level diagram. ω_0 is the central angle frequency of the coupling pulse. Δ_1 , Δ_2 , Δ_3 are the detunings with positive values. **(b)** Experimental setup. The cesium cell is a 75 mm-long cylindrical glass filled with ^{133}Cs atoms and 10 Torr neon as buffer gas, and its temperature is heated up to 61.3 °C. WP Wollaston prism, HWP half-wave plate, QWP quarter-wave plate, PBS polarization beam splitter, APD avalanche photodiode. Transmission properties of the cascaded cavities built for signal **(c)** and idler **(d)** photons. The total full-width at half-maximum (FWHM) of each set of cascaded cavities is around 380 MHz, and their peak transmission efficiencies exceed 70%

short coupling pulse with a detuning of $\Delta_2 + \Delta_3$. In 1969, Mollow found that a single spectral line of a two-level atom driven near resonance by a monochromatic classical electric field can develop to three spectral lines called Mollow-triplet emission spectrum.³¹ The investigation later on suggested that three-level atoms possess richer interference effects. The Mollow-triplet sideband emission from a quantum dot has been used to generate cascaded single photons.³² It is reasonable to consider the light-matter interference in Raman-like system as another counterpart of the Mollow-triplet. The interaction can be regarded as a straightforward model of a light-matter multi-field interference driven by single far off-resonance pulse (see Methods). We can derive the frequency position and relative emission amplitude $|D_j|$ of each spectral component.

In Fig. 2, we show the normalized amplitude $|D_j|$ with four different detunings of the coupling light. Compared with two-level atoms, three-level atoms possess richer interference effects. During the interaction, the strong coupling pulse can induce some virtual energy levels, which is the reason why some extra spectral components appear, for example the component 7 in Fig. 2. The concept of virtual energy level is also used to illustrate the Raman scattering. We select correlated components 2 and 6 as the idler and signal, respectively, for the observation of nonclassical states. The component 1 corresponds to the resonant transition $|2\rangle \rightarrow |1\rangle$. In addition, most of atoms populate in the state $|1\rangle$ (see Fig. 5 in the Methods). There is a strong coupling between the state $|2\rangle$ and state $|1\rangle$. Thus, the component 1 is consistently large.

In contrast, very few atoms populate in the state $|3\rangle$, and hence the component 3 is much smaller, although it corresponds to the resonant transition $|2\rangle \rightarrow |3\rangle$. It means that the amplitude of spectral components depends not only on the detuning but also on the population. In our experiment, we did not choose the components 1 and 3 because they are resonant or near-resonant to the atomic transition line, and therefore inevitably suffer from contamination of fluorescence noises.³³ The component 4 overlaps with the coupling light, while component 5 is considerably small. Both the theoretical and experimental results confirm that $|D_5|$ is vanishingly small. This suggests that the amplitude of the corresponding virtual energy level is much smaller. The detected counts of the component 7 are also much smaller than components 2 and 6 (see Fig. 3a). With Fig. 2, we can also determine that the optimal detuning is around 4 GHz when both signal and idler are far away from the resonant fluorescence.

It will be much more complex to calculate the emission direction and polarization characteristics of each spectral component. In the light of two previous works,^{34,35} we use a high-extinction-ratio Wollaston prism and a single mode fiber to well define the desired polarization and emission direction. The emission direction of the desired correlated photons is coaxial with the coupling light, and their polarizations are perpendicular to that of the coupling light.

As is shown in Fig. 1, by independently setting the central frequency position of two sets of cascaded cavities, we clearly observe the desired idler (blue dot) and signal (red dot) when the

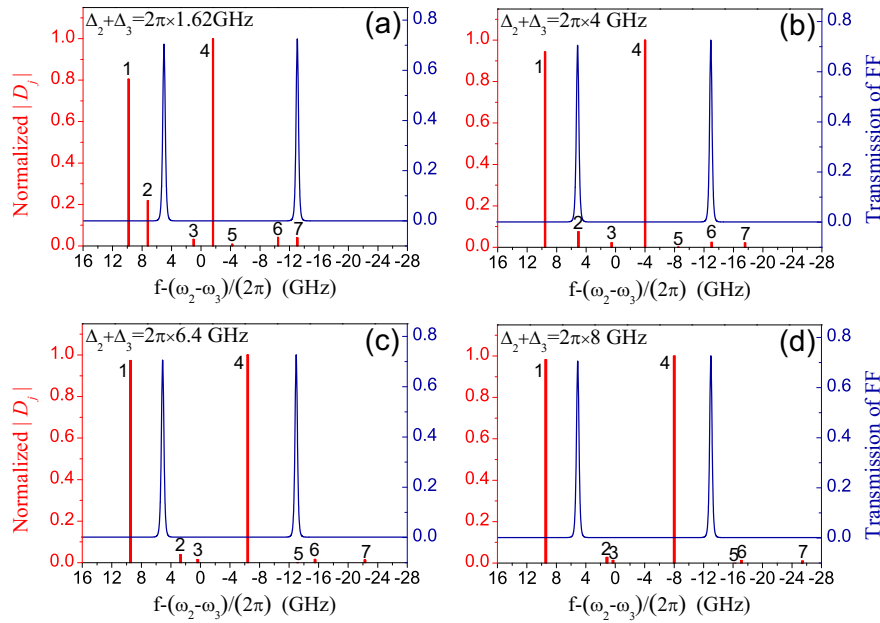


Fig. 2 Emissions of the multi-field interference induced by a single coupling pulse. The normalized components $|D_j|$ with four different detunings of the coupling light and their Y-axis labels are marked in red. The transmission windows of the frequency filter (FF) constituted by cascaded cavities and their Y-axis labels are marked in blue. They are shown together in order to facilitate the selection of emissions and explanation of the observed three-peak phenomena

detuning $\Delta_2 + \Delta_3 = 2\pi \times 4$ GHz. Then we scan the detuning $\Delta_2 + \Delta_3$ while the cascaded cavities remain unchanged, and we can obtain the convolution between the window of cascaded cavities and the desired photons (see Fig. 3a,b). The Peak 1 and Peak 2 correspond to the signal and idler photons, respectively.

In addition to the expected peaks, the appearance of Peak 3 needs to be explained. As we can see in Fig. 2a, when $\Delta_2 + \Delta_3 = 2\pi \times 1.62$ GHz, the component 7 apparently overlaps with one of the transmission windows of the cascaded cavities, which results in the emergence of Peak 3 shown in Fig. 3a. The measured component 7 is much weaker than the component 6, which implies that the polarization or emission direction of component 7 is much different from the desired direction defined by the Wollaston prism and the single mode fiber. The idler and signal photons correspond to the components 2 and 6, respectively, and are designed to maximally pass through cascaded cavities when $\Delta_2 + \Delta_3 = 2\pi \times 4.00$ GHz. For other detunings, such as $2\pi \times 6.40$ GHz and $2\pi \times 8.00$ GHz, there are no any other overlap with the transmission windows of the cascaded cavities. The three peaks that we have observed therefore further confirm our theoretical model.

The bandwidth of the generated photons can be mainly determined by the bandwidth of coupling pulses, Doppler broadening, collision broadening, and AC-Stark effect. In our experiment, while the larger bandwidth of nonclassical states can be achieved by using shorter coupling pulses, it should be smaller than cesium ground state hyperfine splitting of 9.19 GHz. With the measured transmission window of the cascaded cavities shown in Fig. 1c, d and their convolution with the desired photons shown in Fig. 3a, b, we obtain the spectra of the signal and idler photons shown in Fig. 3c, d by applying convolution theorem and Fourier transform. The bandwidths of the signal and idler photons are 590 and 641 MHz, respectively, which confirms the broadband property of the correlated photons that are determined by the pulse duration of the coupling light (2 ns). This observed broadband nonclassical state, associated with a well-defined creation time, is therefore well compatible with Raman¹⁶ and FORD¹⁹ broadband quantum memory for future quantum enhanced applications.

To quantify the nonclassicality of the correlated photons, when the detuning $\Delta_2 + \Delta_3 = 2\pi \times 4$ GHz and the coupling pulse energy 95 pJ, we measure the violation of Cauchy–Schwarz inequality³⁶

$$(g_{\text{SI}}^{(2)})^2 \leq g_{\text{SS}}^{(2)} \cdot g_{\text{II}}^{(2)} \quad (1)$$

where correlation functions can be obtained from the detection probability, for example, the cross correlation $g_{\text{SI}}^{(2)} = p_{\text{SI}} / (p_{\text{S}} \cdot p_{\text{I}})$. The non-heralded auto-correlation of the signal (idler) photons $g_{\text{SS}}^{(2)}$ ($g_{\text{II}}^{(2)}$) is 2.05 ± 0.10 (1.64 ± 0.21), and the cross correlation of the signal and idler photons $g_{\text{SI}}^{(2)}$ is up to 8.58 ± 0.12 . Our measurements lead to a violation of Cauchy–Schwarz inequality up to 568 standard deviations.

In an ideal condition, $g_{\text{SS}}^{(2)} = 2$ and $g_{\text{II}}^{(2)} = 2$. In practice, unwanted multimode couplings and the background noises (such as the leakage of the coupling pulses and dark counts) may decrease the auto-correlation, thus $g_{\text{SS}}^{(2)}$ and $g_{\text{II}}^{(2)}$ may go a bit smaller than 2. Although there always exists a fluctuation around the ideal value due to the instability of the experimental setup, we still find that $g_{\text{SS}}^{(2)} = 2.05 \pm 0.10$ is almost equal to 2 with a measurement uncertainty ± 0.1 based on Poissonian statistics, which means that the noise in the signal channel can be ignored and means a high heralded purity.³⁷ The cross correlation $g_{\text{SI}}^{(2)} > 2$ is a signature of the violation of the Cauchy–Schwarz inequality.⁶ Compared with classical light, the essential feature of non-classical light is that the non-classical photons are correlated with each other, i.e. the detection of the signal photon can herald the existence of the idler photon. The heralded single photon itself is a crucial source for many quantum tasks. With the help of quantum memory, many heralded single photons can be effectively synchronized to multiphoton sources for large-scale quantum information processing. In contrast, the detection of a classical photon, such as a chaotic light or laser, cannot herald the existence of the other photon. That is to say whether or not the other photon comes is completely uncertain, which invalidates the application of quantum memories in photonic networks. Due to the importance of the Cauchy–Schwarz inequality, it is widely used in the field of quantum information.^{7–9}

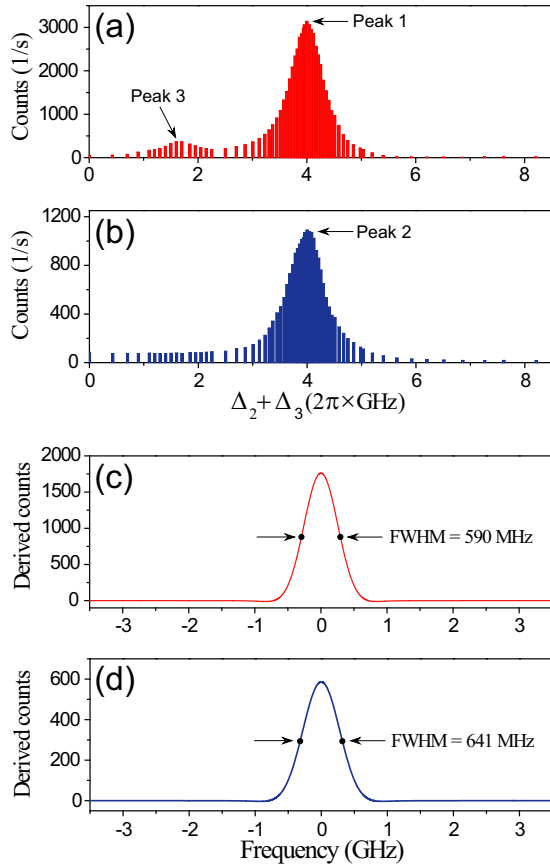


Fig. 3 Experimental results of convolution measurement on the correlated photons. The measured convolution of the signal (a) and idler (b) photons and the windows of cascaded cavities. Peak 1 and Peak 2 correspond to signal and idler photons, respectively. Peak 3 is explained in main text. From the spectra of signal (c) and idler (d) photons, their bandwidths can be derived as 590 and 641 MHz, respectively

In Fig. 4, the measured excitation probability of photon pairs and cross correlation $g_{SI}^{(2)}$ show a tradeoff as a function of the coupling pulse energy. The coupling pulse width is 2 ns, and the width of the arrival time of the generated photons is also about 2 ns. In our experiment, the coincidence window (also known as integration gate) is 9 ns and is centered at the arrival time of the desired photons. If the counting system obtains a signal photon and an idler photon in a same trial (i.e., the two photons are generated by a same coupling pulse), the counting system will record the event which indicates a successful generation of photon pairs. By accumulating a lot of trials, we can obtain the mean number of photon pairs per coupling pulse. The results shown in Fig. 4a have been divided by the square of the total detection efficiency and show the excitation probability originally in the atomic ensemble. The maximum total transmission efficiency of the cascaded cavity filters is about 70% as is shown in Fig. 1 c, d. Based on the spectra of signal and idler photons shown in Fig. 3c,d, we can calculate out the practical transmission efficiency about 40%. Taking collection efficiency of fibers into account, the total transmission efficiency is about 11%. The quantum efficiency of detectors is about 50%. Due to the symmetry of the experimental setup, the total detection efficiency of the signal photons is almost same as that of the idler photons. The total detection efficiency is about 5.5%.

We can see that the cross correlation $g_{SI}^{(2)}$ can reach 17 at a lower excitation probability (see Fig. 4b). For a comparably large excitation probability, $g_{SI}^{(2)}$ all exceed the classical boundary of 2.

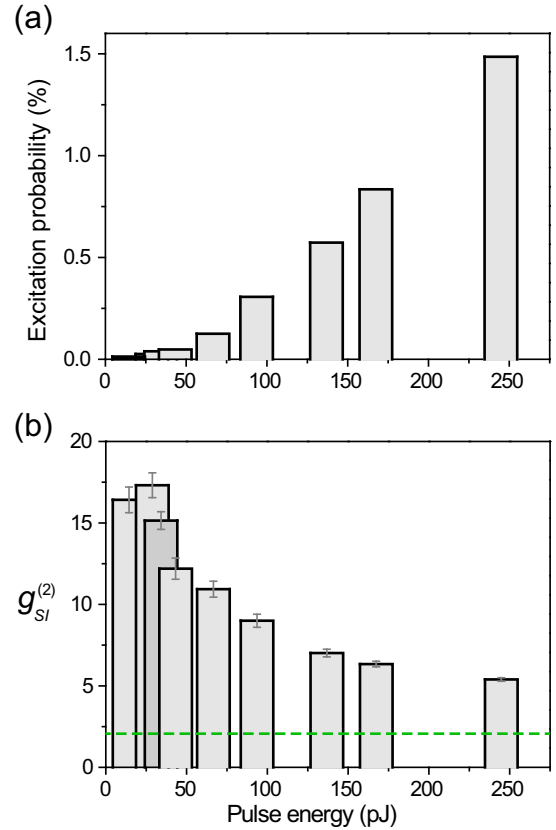


Fig. 4 Nonclassicality excitation tradeoff. Experimental results on excitation probability of photon pairs (a) and cross-correlation function $g_{SI}^{(2)}$ (b) with scanned pulse energy of the coupling light. The detuning is set at $\Delta_1 + \Delta_2 = 2\pi \times 4$ GHz. The results $g_{SI}^{(2)}$ larger than 2 (green dashed) is in nonclassical regime. The beam waist of the coupling light is 90 μm . The coincidence window (also known as integration gate) is 9 ns and is centered at the arrival time of the desired photons. Error bars are given by Poissonian statistics

There is a probability that the emitted photons are re-absorbed, which is called radiation trapping.³⁸ It is a common phenomenon in various light-matter interaction processes. However, to obtain high-quality nonclassical states, we only need to care about the effective excitation probability. We also experimentally investigate the time dependence properties of cross correlation (see Methods).

For a photon pair, p_{SI}/p_S is the heralding efficiency for idler photons. In our experiment, the heralding efficiency changes from 1.5% to 16% as the excitation probability (photon pairs per coupling pulse) changes from 0.013% to 1.49%. The probability p_I of idler photons changes from 0.09% to 3.0%. We can see that the growth rate of the probability p_I is higher than that of the heralding efficiency, therefore results in a decrease of the cross correlation shown in Fig. 4b. When the idler photons is used as the herald, then the heralding efficiency is given by p_{SI}/p_I which changes from 14% to 50% as the excitation probability changes from 0.013% to 1.49%. Thus, we can get a considerably larger heralding efficiency when the idler photons is the herald.

It is worth mentioning that the pump light used to prepare the atoms in initial state $|1\rangle$ is necessary for achieving the nonclassicality. Without the pump light, the cross correlation $g_{SI}^{(2)}$ degrades to 1.62 ± 0.04 , i.e., the nonclassicality disappears. If the ground state is unpumped, atoms almost equally populate in state $|1\rangle$ and state $|3\rangle$. A coupling pulse does not only excite photons from state $|1\rangle$ but also from state $|3\rangle$, and the two processes are independent to each other, i.e. the photons from the state $|1\rangle$

have no correlation with that from the state $|3\rangle$. Thus, the non-classicality disappears when the ground state is unpumped. In an ideal condition, the purity of the initial state should be 100%, i.e., all of the atoms populate on the energy level $|1\rangle$ after the pumping process, which is challenging for warm atoms. We use a pump light with a power of 16.4 mW and a pump time of 1.2 μ s. The beam waist of the pump light is about 2500 μ m. We use a very weak and counter-propagated probe pulse (pulse duration 300 ns, beam waist 140 μ m) to measure the polarization purity. Since the pumped region is one order larger than the probe region, and the time delay of 300 ns between the probe pulse and the turnoff of the pumping light is so short that the unpumped atoms outside the pumped region cannot enter the probe region. We finally achieve a purity of the initial state up to 90%.

DISCUSSION

In summary, we propose and experimentally demonstrate a multi-field interference between light and atoms with single coupling pulse and far off-resonance configuration. With this we achieve the direct observation of broadband nonclassical states in a room-temperature light-matter interface, where the atoms can also be controlled to store and interfere with photons. The obtained nonclassical states are compatible and therefore can be directly used to interfere with broadband off-resonance quantum memories.^{16,19}

To be compatible with large-scale fiber networks, the near-infrared wavelength around 852 nm of the obtained nonclassical state can be converted to telecommunication wavelength by using the cascade schemes^{39,40} or on-chip frequency converters.^{41–43}

The measured strong nonclassicality associated with low noise level reveals the potential of the collinear configuration, in which the created photons are coaxial with the coupling light, for both broadband state generations and quantum memories in room-temperature atoms. This is particularly important for the architectures based on DLCZ protocols^{10,11,28,34,44,45} as the emitted photons correlated with the spin waves stored in the quantum memory are mainly inside a small cone around the direction of the write light.³⁴ Hence, a collinear configuration means the highest collection efficiency of write-out photons. Additionally, a collinear configuration possesses a maximum wavelength of spin waves and therefore a longer storage lifetime against dephasing.⁴⁶

METHODS

A light-matter multi-field interference driven by single far off-resonance pulse

The total Hamiltonian of atoms can be written as

$$H = H_0 + H_I \quad (2)$$

where $H_0|n\rangle = \hbar\omega_n|n\rangle$ with $n=1,2,3$ and interaction term is $H_I = e\vec{R} \cdot \vec{E}$. The vector \vec{R} is the position of the outermost electron of Cs, and $\vec{E} = \frac{1}{2}\vec{A}(\vec{r}, t)[\exp(-i\omega_0 t) + \exp(i\omega_0 t)]$ denotes the coupling light. The wave function $\psi(\vec{r}, t)$ of atoms affected by coupling light can be expanded in terms of the eigenfunction $|n\rangle$ of bare atoms.

$$\psi(\vec{r}, t) = \sum_{n=1}^3 \{C_n(t)|n\rangle \exp[-i\omega_n t + (-1)^n i\Delta_n t]\} \quad (3)$$

By using rotating-wave approximation, the Schrödinger equation $i\hbar \frac{\partial \psi(\vec{r}, t)}{\partial t} = H\psi(\vec{r}, t)$ can be expressed as a form of matrices

$$i\hbar \frac{\partial}{\partial t} \begin{pmatrix} C_1 \\ C_2 \\ C_3 \end{pmatrix} = \frac{\hbar}{2} \begin{pmatrix} -2\Delta_1 & \Omega_{12} & 0 \\ \Omega_{21} & 2\Delta_2 & \Omega_{23} \\ 0 & \Omega_{32} & -2\Delta_3 \end{pmatrix} \begin{pmatrix} C_1 \\ C_2 \\ C_3 \end{pmatrix} \quad (4)$$

where $\Omega_{mn} = \langle m|\vec{e}\vec{R} \cdot \vec{A}|n\rangle/\hbar$. For simplicity, the space-time-dependent Ω_{mn} can be replaced by its effective value.

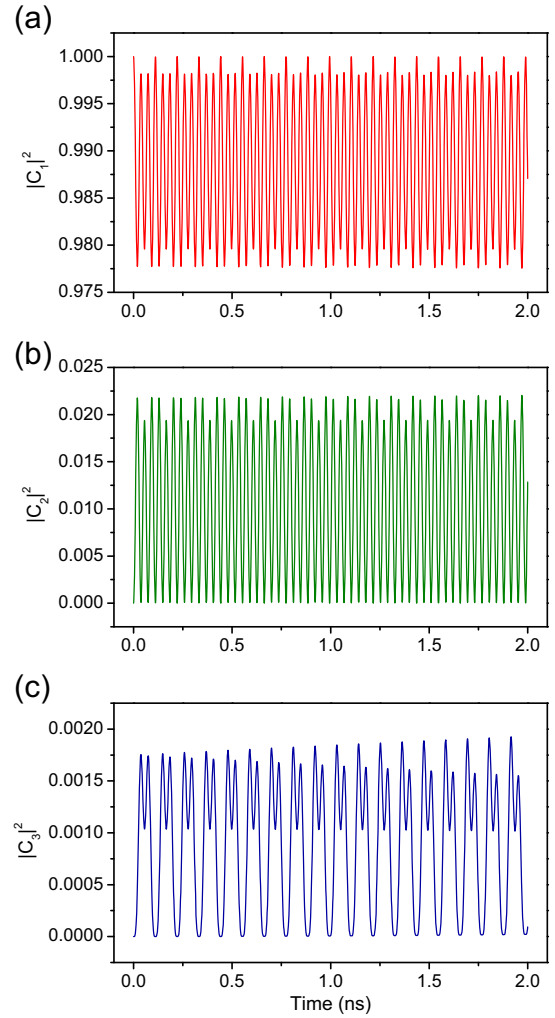


Fig. 5 The population of energy levels. For a straightforward clarification, we use a square-pulse model (i.e., the pulse intensity is a constant during the interval of 2 ns) to calculate the population coefficients $|C_1|^2$, $|C_2|^2$, and $|C_3|^2$. The main information we can get is the dominant population of atoms. We also can see a transient optical effect associated with rapid oscillations before the superposition states decay to equilibrium states

Suppose that the eigenstates of the matrix

$$\frac{\hbar}{2} \begin{pmatrix} -2\Delta_1 & \Omega_{12} & 0 \\ \Omega_{21} & 2\Delta_2 & \Omega_{23} \\ 0 & \Omega_{32} & -2\Delta_3 \end{pmatrix} \quad (5)$$

is

$$\begin{pmatrix} f_n \\ g_n \\ h_n \end{pmatrix} \exp(-i\lambda_n t), \quad (6)$$

where $n=1,2,3$ and

$$\begin{pmatrix} f_n \\ g_n \\ h_n \end{pmatrix} \quad (7)$$

is independent of time t . With the matrix (5), (6) and a Schrödinger equation, we can obtain the following equation:

$$\frac{\hbar}{2} \begin{pmatrix} -2\Delta_1 - 2\lambda_n & \Omega_{12} \\ \Omega_{21} & 2\Delta_2 - 2\lambda_n & \Omega_{23} \\ \Omega_{32} & -2\Delta_3 - 2\lambda_n \end{pmatrix} \begin{pmatrix} f_n \\ g_n \\ h_n \end{pmatrix} \exp(-i\lambda_n t) = 0. \quad (8)$$

Based on this equation, the eigenstates and eigenvalues can be calculated out.

Suppose $C_n = a_n \exp[(-1)^n i \Delta_n t]$. The expansion coefficients a_n can be expressed in terms of the eigenstates of the matrix (5).

$$\begin{pmatrix} a_1 \\ a_2 \\ a_3 \end{pmatrix} = \sum_{n=1}^3 \left\{ q_n \begin{pmatrix} f_n \\ g_n \\ h_n \end{pmatrix} \exp(-i \lambda_n t) \right\} = \begin{pmatrix} G_{11} & G_{12} & G_{13} \\ G_{21} & G_{22} & G_{23} \\ G_{31} & G_{32} & G_{33} \end{pmatrix} \begin{pmatrix} \exp(-i \lambda_1 t) \\ \exp(-i \lambda_2 t) \\ \exp(-i \lambda_3 t) \end{pmatrix} \quad (9)$$

where q_n and G_{mn} are expansion coefficients. Note that the coefficients $C_1 = 1, C_2 = 0, C_3 = 0$ at initial time ($t = 0$). Then, we can calculate out the expansion coefficients G_{mn} and obtain the wave function ψ .

$$\begin{aligned} \psi &= \sum_{n=1}^3 [C_n(t) |n\rangle \exp(-i \omega_n t)] \\ &= |1\rangle \{G_{11} \exp[-i(\omega_1 + \Delta_1 + \lambda_1)t] + G_{12} \exp[-i(\omega_1 + \Delta_1 + \lambda_2)t] + G_{13} \exp[-i(\omega_1 + \Delta_1 + \lambda_3)t]\} \\ &\quad + |2\rangle \{G_{21} \exp[-i(\omega_2 - \Delta_2 + \lambda_1)t] + G_{22} \exp[-i(\omega_2 - \Delta_2 + \lambda_2)t] + G_{23} \exp[-i(\omega_2 - \Delta_2 + \lambda_3)t]\} \\ &\quad + |3\rangle \{G_{31} \exp[-i(\omega_3 + \Delta_3 + \lambda_1)t] + G_{32} \exp[-i(\omega_3 + \Delta_3 + \lambda_2)t] + G_{33} \exp[-i(\omega_3 + \Delta_3 + \lambda_3)t]\} \end{aligned} \quad (10)$$

Initially, atoms are prepared in state $|1\rangle$. However, during the light-matter interaction process, the population of each energy level will change, and the bare states will change to a coherent superposition state ψ as is shown above. Figure 5a–c show the population of the energy level $|1\rangle$, $|2\rangle$, and $|3\rangle$, respectively. We can see that most atoms populate on the level $|1\rangle$. There is a rapid oscillation in the population, which is called the transient optical effect. If the decay for every energy level is considered, the rapid oscillation will behave damped and the superposition state ψ will finally become an equilibrium state which is independent of time. In our experiment, the interaction time is so short (about 2 ns) that the decay effect is not taken into account.

The expectation value of the dipole moment is

$$\begin{aligned} \langle \psi | ex | \psi \rangle &= D_1 \exp[-i(\omega_0 + \lambda_2 - \lambda_1)t] \\ &\quad + D_2 \exp[-i(\omega_0 + \lambda_3 - \lambda_1)t] \\ &\quad + D_3 \exp[-i(\omega_0 + \lambda_2 - \lambda_3)t] \\ &\quad + D_4 \exp(-i \omega_0 t) \\ &\quad + D_5 \exp[-i(\omega_0 + \lambda_3 - \lambda_2)t] \\ &\quad + D_6 \exp[-i(\omega_0 + \lambda_1 - \lambda_3)t] \\ &\quad + D_7 \exp[-i(\omega_0 + \lambda_1 - \lambda_2)t] \\ &\quad + \text{c.c.} \end{aligned} \quad (11)$$

where x is the projection of \vec{R} on the polarization direction of the coupling light, and D_i denotes the relative amplitude of the corresponding spectral component.

$$\begin{pmatrix} D_1 \\ D_2 \\ D_3 \\ D_4 \\ D_5 \\ D_6 \\ D_7 \end{pmatrix} = \begin{pmatrix} d_{12} G_{11} G_{22} + d_{32} G_{31} G_{22} \\ d_{12} G_{11} G_{23} + d_{32} G_{31} G_{23} \\ d_{12} G_{13} G_{22} + d_{32} G_{33} G_{22} \\ d_{12} [G_{11} G_{21} + G_{12} G_{22} + G_{13} G_{23}] + d_{32} [G_{31} G_{21} + G_{32} G_{22} + G_{33} G_{23}] \\ d_{12} G_{12} G_{23} + d_{32} G_{32} G_{23} \\ d_{12} G_{13} G_{21} + d_{32} G_{33} G_{21} \\ d_{12} G_{12} G_{21} + d_{32} G_{32} G_{21} \end{pmatrix} \quad (12)$$

where $d_{mn} = \langle m | ex | n \rangle$ is the effective dipole moment corresponds to the transtion $|n\rangle \rightarrow |m\rangle$. So far, we have derived the frequency position and relative emission amplitude of each spectral component with a straightforward model. Initially, atoms are prepared in state $|1\rangle$. The photons stem from a same initial state, which is a necessary condition for generation of non-classical correlation. And not only that, there should also exists a bunching effect for the emissions of the signal and idler photons.⁴⁷

In addition, during the light-matter interference, there exists AC-Stark shift of the energy level, i.e. the detuning Δ_n will change to $(-1)^n \lambda_n$. The AC-Stark shift of the state $|n\rangle$ is equal to $[(-1)^n \times \lambda_n - \Delta_n]$, which is on the order of $2\pi \times 100$ MHz in our experiment. It is very straightforward to

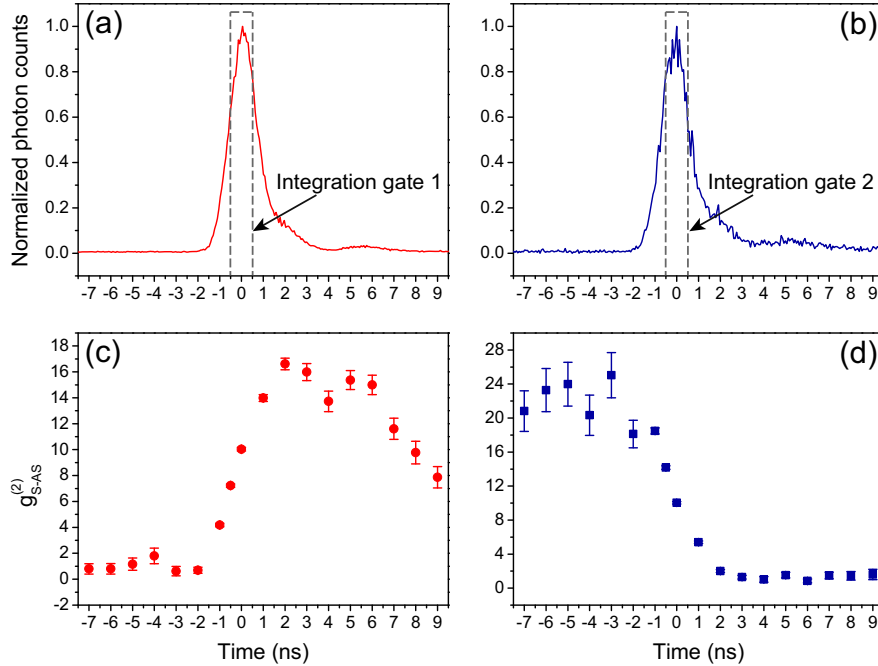


Fig. 6 The time dependence of cross correlation. (a) and (b) show the normalized photon counts of signal photons and idler photons, respectively. By scanning the delay of the integration gate 2, we obtain (c) while the integration gate 1 is centered at 0 ns. By scanning the delay of the integration gate 1, we obtain (d) while the integration gate 2 is centered at 0 ns. The beam waist is 200 μm , and the pulse energy is 225 pJ

calculate the AC-Stark shift of each state, which is the reason why we depict the detuning in the unusual way as is shown in Fig. 1a.

Measurement of time dependence of cross correlation

The detection system always has a minimum resolving time and a minimum coincidence window (also known as integration gate). The results in Fig. 4 are obtained by setting a 9-ns integration gates centered at the arrival time of the desired photons. In order to measure the time dependence of cross correlation, we employ a new counting system whose resolving time is shorter than 1 ns and the integration gate is 1 ns.

The new experiment reveals more interesting dynamic properties of the light-matter interference. Figure 6a,b show the normalized photon counts of signal photons and idler photons, respectively. In Fig. 6a,b, the delay of the two integration gates is 0 ns. By scanning the delay of the integration gate 2, we obtain Fig. 6c while the integration gate 1 is centered at 0 ns. Similarly, we obtain Fig. 6d by scanning the delay of the integration gate 1 while the integration gate 2 is centered at 0 ns. In the time region around 0 ns, there is a monotone zone of the cross correlation. A higher cross correlation can be obtained when the integration gate 1 is ahead of the integration gate 2. In contrast, the cross correlation is lower when the integration gate 2 is ahead of the integration gate 1. This monotone zone implies that the generation time of idler photons is posterior to that of the correlated signal photons. Thus, there is a cascaded-like emission of photon pairs.

In our experiment, the switching extinction ratio of the coupling light is several hundreds, which means the coupling light is not absolutely zero when it should have been switched off. The non-zero coupling light may excite signal or idler photons in the time region far away from 0 ns, of course in a very low probability. We can see that the statistic error bar of the data far away from 0 ns is much larger than that around 0 ns, which means a very low excitation probability when either of the integration gates is set far away from 0 ns.

Data availability

The data that support the findings of this study are available from the corresponding author on request.

ACKNOWLEDGEMENTS

The authors thank J.-W. Pan for helpful discussions. This work was supported by National Key R&D Program of China (2017YFA0303700); National Natural Science Foundation of China (NSFC) (11374211, 61734005, 11690033); Shanghai Municipal Education Commission (SMEC)(16SG09, 2017-01-07-00-02-E00049); Science and Technology Commission of Shanghai Municipality (STCSM) (15QA1402200, 16JC1400405); Open fund from HPCL (201511-01). X.-M.J. acknowledges support from the National Young 1000 Talents Plan.

AUTHOR CONTRIBUTIONS

X.-M.J. conceived the project. J.-P.D. and X.-M.J. designed the experiment. J.-P.D., A.-L. Y., M.-Y.D., D.L., H.L., X.-L.P., J.G., L.-F.Q., H.T. performed the experiment. J.-P.D. developed the theory. X.-M.J. and J.-P.D. analyzed the data and wrote the paper.

ADDITIONAL INFORMATION

Competing interests: The authors declare no competing interests.

Publisher's note: Springer Nature remains neutral with regard to jurisdictional claims in published maps and institutional affiliations.

REFERENCES

- O'Brien, J. L., Furusawa, A. & Vučković, J. Photonic quantum technologies. *Nat. Photon.* **3**, 687–695 (2009).
- Gisin, N. & Thew, R. Quantum communication. *Nat. Photon.* **1**, 165–171 (2007).
- Ladd, T. D. et al. Quantum computers. *Nature* **464**, 45–53 (2010).
- Aspuru-Guzik, A. & Walther, P. Photonic quantum simulators. *Nat. Phys.* **8**, 285–291 (2012).
- Lvovsky, A. I., Sanders, B. C. & Tittel, W. Optical quantum memory. *Nat. Photon.* **3**, 706–714 (2009).
- Sangouard, N., Simon, C., de Riedmatten, H. & Gisin, N. Quantum repeaters based on atomic ensembles and linear optics. *Rev. Mod. Phys.* **83**, 33–80 (2011).
- Chanelière, T. et al. Storage and retrieval of single photons transmitted between remote quantum memories. *Nature* **438**, 833–836 (2005).
- Eisaman, M. D. et al. Electromagnetically induced transparency with tunable single-photon pulses. *Nature* **438**, 837–841 (2005).
- Zhang, H. et al. Preparation and storage of frequency-uncorrelated entangled photons from cavity-enhanced spontaneous parametric downconversion. *Nat. Photon.* **5**, 628–632 (2011).
- Kuzmich, A. et al. Generation of nonclassical photon pairs for scalable quantum communication with atomic ensembles. *Nature* **423**, 731–734 (2003).
- Chrapkiewicz, R., Dabrowski, M. & Wasilewski, W. High-capacity angularly multiplexed holographic memory operating at the single-photon level. *Phys. Rev. Lett.* **118**, 063603 (2017).
- Julsgaard, B., Sherson, J., Cirac, J. I., Fiurášek, J. & Polzik, E. S. Experimental demonstration of quantum memory for light. *Nature* **432**, 482–486 (2004).
- Alexander, A. L., Longdell, J. J., Sellars, M. J. & Manson, N. B. Photon echoes produced by switching electric fields. *Phys. Rev. Lett.* **96**, 043602 (2006).
- Afzelius, M., Simon, C., de Riedmatten, H. & Gisin, N. Multimode quantum memory based on atomic frequency combs. *Phys. Rev. A* **79**, 052329 (2009).
- Hosseini, M., Sparkes, B. M., Campbell, G., Lam, P. K. & Buchler, B. C. High efficiency coherent optical memory with warm rubidium vapour. *Nat. Commun.* **2**, 174 (2011).
- Reim, K. F. et al. Multi-pulse addressing of a Raman quantum memory: configurable beam splitting and efficient readout. *Phys. Rev. Lett.* **108**, 263602 (2012).
- Ding, D.-S. et al. Raman quantum memory of photonic polarized entanglement. *Nat. Photon.* **9**, 332–338 (2015).
- Kaczmarek, K. T. et al. High-speed noise-free optical quantum memory. *Phys. Rev. A* **97**, 042316 (2018).
- Dou, J.-P. et al. A broadband DLCZ quantum memory in room-temperature atoms. Preprint at arXiv:1704.06309 (2017).
- Ou, Z. Y. & Lu, Y. J. Cavity enhanced spontaneous parametric down-conversion for the prolongation of correlation time between conjugate photons. *Phys. Rev. Lett.* **83**, 2556–2559 (1999).
- Kuklewicz, C. E., Wong, F. N. C. & Shapiro, J. H. Time-bin-modulated biphotons from cavity-enhanced down-conversion. *Phys. Rev. Lett.* **97**, 223601 (2006).
- Chou, C. W., Polyakov, S. V., Kuzmich, A. & Kimble, H. J. Single-photon generation from stored excitation in an atomic ensemble. *Phys. Rev. Lett.* **92**, 213601 (2004).
- Thompson, J. K., Simon, J., Loh, H. & Vuletić, V. A high-brightness source of narrowband, identical-photon pairs. *Science* **313**, 74–77 (2006).
- Srivathsan, B. et al. Narrow band source of transform-limited photon pairs via four-wave mixing in a cold atomic ensemble. *Phys. Rev. Lett.* **111**, 123602 (2013).
- Shu, C. et al. Subnatural-linewidth biphotons from a Doppler-broadened hot atomic vapour cell. *Nat. Commun.* **7**, 12783 (2016).
- van der Wal, C. H. et al. Atomic memory for correlated photon states. *Science* **301**, 196–200 (2003).
- Manz, S., Fernholz, T., Schmiedmayer, J. & Pan, J.-W. Collisional decoherence during writing and reading quantum states. *Phys. Rev. A* **75**, 040101(R) (2007).
- Bashkansky, M. et al. Quantum memory in warm rubidium vapor with buffer gas. *Opt. Lett.* **37**, 142–144 (2012).
- Willis, R. T., Becerra, F. E., Orozco, L. A. & Rolston, S. L. Correlated photon pairs generated from a warm atomic ensemble. *Phys. Rev. A* **82**, 053842 (2010).
- Ding, D.-S. et al. Generation of non-classical correlated photon pairs via a ladder-type atomic configuration: theory and experiment. *Opt. Express* **20**, 11433–11444 (2012).
- Mollow, B. R. Power spectrum of light scattered by two-level systems. *Phys. Rev.* **188**, 1969–1975 (1969).
- Ulhaq, A. et al. Cascaded single-photon emission from the Mollow triplet sidebands of a quantum dot. *Nat. Photon.* **6**, 238–242 (2012).
- Hsu, M. T. L. et al. Quantum study of information delay in electromagnetically induced transparency. *Phys. Rev. Lett.* **97**, 183601 (2006).
- Duan, L.-M., Cirac, J. I. & Zoller, P. Three-dimensional theory for interaction between atomic ensembles and free-space light. *Phys. Rev. A* **66**, 023818 (2002).
- Nunn, J. *Quantum Memory in Atomic Ensembles*. Ph.D. thesis, University of Oxford (2008).
- Clauser, J. F. Experimental distinction between the quantum and classical field-theoretic predictions for the photoelectric effect. *Phys. Rev. D* **9**, 853–860 (1974).
- Spring, J. B. et al. On-chip low loss heralded source of pure single photons. *Opt. Express* **21**, 13522 (2013).
- Thomas, S. E. et al. High efficiency Raman memory by suppressing radiation trapping. *New J. Phys.* **19**, 063034 (2017).
- Radnaev, A. G. et al. A quantum memory with telecom-wavelength conversion. *Nat. Phys.* **6**, 894–899 (2010).
- Dudin, Y. O. et al. Entanglement of light-shift compensated atomic spinwaves with telecom light. *Phys. Rev. Lett.* **105**, 260502 (2010).

- 8
41. Albrecht, B. et al. A waveguide frequency converter connecting rubidium-based quantum memories to the telecom C-band. *Nat. Commun.* **5**, 3376 (2014).
 42. Farrera, P. et al. Nonclassical correlations between a C-band telecom photon and a stored spin-wave. *Optica* **3**, 1019–1024 (2016).
 43. Ikuta, R. et al. Heralded single excitation of atomic ensemble via solid-state-based telecom photon detection. *Optica* **3**, 1279–1284 (2016).
 44. Duan, L.-M., Lukin, M. D., Cirac, J. I. & Zoller, P. Long-distance quantum communication with atomic ensembles and linear optics. *Nature* **414**, 413–418 (2001).
 45. Namazi, M. et al. Ultra-low-noise room-temperature quantum memory for polarization qubits. *Phys. Rev. Appl.* **8**, 034023 (2017).
 46. Zhao, B. et al. A millisecond quantum memory for scalable quantum networks. *Nat. Phys.* **5**, 95–99 (2009).
 47. Nienhuis, G. Spectral correlations in resonance fluorescence. *Phys. Rev. A* **47**, 510–518 (1993).



Open Access This article is licensed under a Creative Commons Attribution 4.0 International License, which permits use, sharing, adaptation, distribution and reproduction in any medium or format, as long as you give appropriate credit to the original author(s) and the source, provide a link to the Creative Commons license, and indicate if changes were made. The images or other third party material in this article are included in the article's Creative Commons license, unless indicated otherwise in a credit line to the material. If material is not included in the article's Creative Commons license and your intended use is not permitted by statutory regulation or exceeds the permitted use, you will need to obtain permission directly from the copyright holder. To view a copy of this license, visit <http://creativecommons.org/licenses/by/4.0/>.

© The Author(s) 2018